

ARTICLE OPEN



Influence of cementite coarsening on the corrosion resistance of high strength low alloy steel

Chao Liu^{1,2}, Can Li^{1,2}, Zhichao Che³, Xuan Li^{1,2}, Shufeng Yang^{3✉}, Zhiyong Liu^{1,2}, Yigang Zhou⁴ and Xuequn Cheng^{1,2}

The impact of heat treatment on the initiation and progression of localized corrosion in E690 steel in a simulated marine environment was investigated systematically. The primary cause of localized corrosion was the presence of inclusions, which led to the dissolution of the distorted matrix surrounding them. In the initial stages of corrosion, localized corrosion resulting from inclusions was the predominant form. The chemical and electrochemical mechanisms underlying matrix deformation and localized corrosion caused by inclusions were meticulously elucidated. As the immersion time was extended, the galvanic contributions at the ferrite-austenite interfaces, as well as the coarsened carbides, reduced the polarization resistance in the annealed specimen, accelerating the corrosion rate compared to the lath martensite in the as-received specimen. Consequently, the heat-treated sample promoted a transition from localized to uniform corrosion. Finally, a model was established to describe the corrosion behavior of E690 steel in the marine environment.

npj Materials Degradation (2023)7:43; <https://doi.org/10.1038/s41529-023-00358-1>

INTRODUCTION

High strength low alloy steels are widely used in ocean engineering equipment^{1–3}. Corrosion threatens the safety and service life of such equipment. In particular, localized corrosion often causes serious and costly damages⁴. The main way to connect marine engineering structures of steel is welding, during which the steel microstructure becomes coarsened under the high energy input^{5–7}. This would profoundly affect the material's corrosion resistance properties.

Previous research found that inclusions play a major role in the initiation of localized corrosion^{8–13}, which starts with the dissolution of inclusions or the adjacent matrix. Some researchers have classified inclusions (e.g., Al_2O_3 ¹⁴, $\text{MnS-Al}_2\text{O}_3$ ¹⁵, $(\text{Ti}, \text{Nb})\text{N}$ ¹⁶, $(\text{Ca}, \text{Mn})\text{S}-(\text{Mg}, \text{Al})\text{O}$ ¹⁷, $\text{MnCr}_2\text{O}_4/\text{MnS}$ ¹⁸, and YS ¹⁹) into a cathode phase and an anode phase. The cathodic or anodic effect of the inclusions has been mainly identified based on local electrochemical measurements such as localized electrochemical impedance spectroscopy¹⁴, Volta potential^{13,16}, energy gap¹⁹, as well as the morphological state of inclusions on the corroded surface^{15,18}. Moreover, our previous research proved that it is impossible to form a galvanic couple between an insulating inclusion (e.g., Al_2O_3 ⁹, $(\text{RE})\text{AlO}_3-(\text{RE})_2\text{O}_2\text{S}-(\text{RE})_x\text{S}_y$ ^{11,20}, and $\text{ZrO}_2-\text{Ti}_2\text{O}_3-\text{Al}_2\text{O}_3$) and the adjacent matrix⁸. We established a corrosion mechanism that includes the effect of lattice distortion and microreverses. Namely, the adjacent matrix with a high density of lattice distortion has higher corrosion activity. So, localized corrosion could initiate there and extend easily^{9,21}. After the matrix dissolves, the formation of oxygen concentration cell and catalytically occluded cell would accelerate the localized corrosion initiation process¹¹. To improve its weldability, steel will be Al-Mg composite deoxidized in the smelting process. This step results in inclusions in the steel, such as $\text{CaS-xMgO-yAl}_2\text{O}_3$ and $\text{CaS-xMgO-yAl}_2\text{O}_3\text{-TiN}$. However, the influence of heat during the welding on the mechanism of localized corrosion induced by these complex inclusions is still unclear.

In aggressive environments, corrosion spots are formed around the micro-pits induced by inclusions^{22–24}. The formation of these corrosion spots is associated with the diffusion of corrosion products. The material's microstructure and the service environment significantly impact the evolution of corrosion spots. Under high hydrostatic pressures, corrosion spots induced by inclusions on the surface of high-strength steel exhibit a higher coalescence rate, which leads to fast and uniform corrosion²². In stainless steel, the corrosion spots would grow sustainably in the longitudinal direction and form stable pits instead²⁴. In a deaerated acidic soil environment, the corrosion spots were found to be protected as the cathodic phase surrounding the pits induced by CaS incision. This protected area would remain attached after the CaS inclusion was totally dissolved¹⁰. We expect corrosion spots to form around inclusions in high-strength low alloy steel under the marine environment. The evolution of these corrosion spots would be a key issue, which plays an important role in revealing the mechanism of corrosion development.

Heat treatment coarsens the microstructures, attenuates the dislocation density, and even changes the type of microstructures. These alterations are known to have different effects on the corrosion activity. For example, the ferrite-pearlite phase with a higher carbon content was reported to exhibit a higher corrosion rate²⁵. The retained austenite would also accelerate the corrosion process via microscopic galvanic contributions at ferrite-austenite interfaces²⁶. What is more, the accumulation of carbides would also accelerate corrosion^{27,28}. Heat treatment could decrease the dislocation density in martensitic steel, but the precipitation of alloy carbides tends to accelerate corrosion²⁹. Unfortunately, there is no in-depth study on how the microstructure changes caused by heat treatment affect the germination and evolution of high strength low alloy steel corrosion.

In this work, we compare the initiation and evolution of corrosion in E690 steel with/without heat treatment in a marine environment. In particular, the mechanism of localized corrosion

¹Institute of Advanced Materials & Technology, University of Science and Technology Beijing, Beijing 100083, PR China. ²National Materials Corrosion and Protection Data Center, University of Science and Technology Beijing, Beijing 100083, PR China. ³School of Metallurgical and Ecological Engineering, University of Science and Technology Beijing, Beijing 100083, PR China. ⁴Peking University library, Peking University, Beijing 100080, PR China. ✉email: yangshufeng@ustb.edu.cn

induced by different types of inclusions was examined using field emission scanning electron microscopy-energy dispersive spectroscopy (FE-SEM-EDS) and electron backscattered diffraction (EBSD). The corrosion was monitored using electrochemical polarization measurement, electrochemical impedance spectroscopy (EIS), and corrosion dynamic analysis.

RESULTS AND DISCUSSION

Microstructure of steel specimens

Morphologies of E690 steel in both the as-received and annealed conditions are displayed in Fig. 1. The as-received material was clearly made of fine-grained bainite laths (Fig. 1a, b), with a large amount of tiny secondary phases uniformly distributed inside the grain (Fig. 1c). The TEM image in Fig. 1g shows obvious bainite plate lath. The bainite laths were ~340 nm in width. The nanoscale secondary phases were identified as cementite (Fe_3C). All cementite precipitates were observed within the martensite laths and at the lath/grain boundaries. Similar precipitates were reported by other researchers²⁹. In contrast, the annealed E690 steel consisted of polygonal ferrite and degenerate pearlite (Fig. 1d), and there were many coarse secondary phases inside the steel (Fig. 1e). As the coarse secondary phases gather, some degenerate pearlite could be seen inside the annealed steel grain (Fig. 1f). The coarsening of the secondary phases was also verified by TEM observations (Fig. 1h). The size of the coarse secondary phases could increase to 670 nm, which is much larger than those in the as-received steel. These larger-sized secondary phases are also mainly Fe_3C . The observed microstructures and precipitates agree with previous reports^{30,31}.

The inverse pole figure, grain orientation, and kernel average misorientation (KAM) of the steel specimens were obtained via EBSD (Fig. 2). In both types of steel, the grain direction is crystallographically homogeneous (Fig. 2a, b). Grains inside the

as-received steel are irregular due to rapid heating and cooling in the hot rolling process. In the annealed steel, the average grain size became as large as 75.32 μm , which is almost nine times that of the as-received sample (Fig. 2c). The annealed steel exhibited straight grain boundaries and some annealed twins due to its full recrystallization³². High-angle grain boundaries (HAGB) (50° – 65° , especially at 60°) in the steel increased significantly after annealing. Accordingly, the percentage of low-angle grain boundaries (LAGB) was relatively lower in the annealed sample. The HAGB is generally considered to have higher energy than the LAGB^{33–35}. The KAM maps (Fig. 2e, g) indicate that the as-received sample had a higher dislocation density than the annealed one, indicating that the former is in a state with higher stress. In comparison, a relatively lower dislocation density was observed inside the annealed specimen (Fig. 2f).

This difference could be ascribed to the high dislocation density accompanying the formation of sub-grains during the crystallization process^{21,36}. In the hot rolling process, carbon is trapped within the body-centered cubic unit cells, giving rise to a tetragonal field that strongly interacts with the dislocation strain fields. Such a bainitic microstructure contains abundant point and line lattice defects³⁷. During annealing, the carbide precipitates gradually coarsen, and the dislocation density decreases at the same time³⁸.

In the low alloy steel, inclusions are generally the initiation points of localized corrosion^{12,16,20}. Figure 3 shows inclusions in the as-received and annealed E690 steel. Because the heat treatment temperature selected in the research was far below the liquefaction temperature of the inclusions, there was no change in the inclusion composition. The main component of the inclusions was $\text{CaS}\cdot\text{xMgO}\cdot\text{yAl}_2\text{O}_3$ (Fig. 3a, c)^{39,40}. A small amount of inclusions made of $\text{CaS}\cdot\text{xMgO}\cdot\text{yAl}_2\text{O}_3\cdot\text{TiN}$ were also detected in the as-received (Fig. 3b) and annealed (Fig. 3d) specimens, probably generated during the calcium treatment of steel^{41–43}.

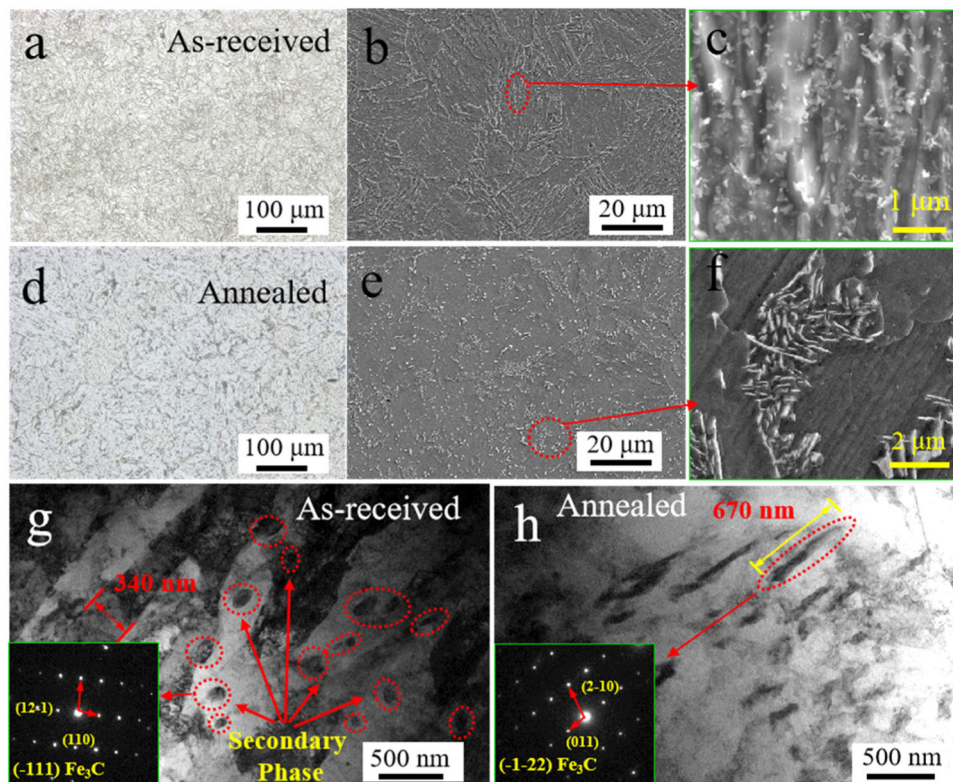


Fig. 1 Microstructure morphology of two experimental E690 steels. **a, d** Stereomicroscopic images, **b, c, e, f** SEM images, and **g, h** TEM morphologies of E690 steel specimens. **a, b, c, g** As-received steel, **d, e, f, h**: annealed steel.

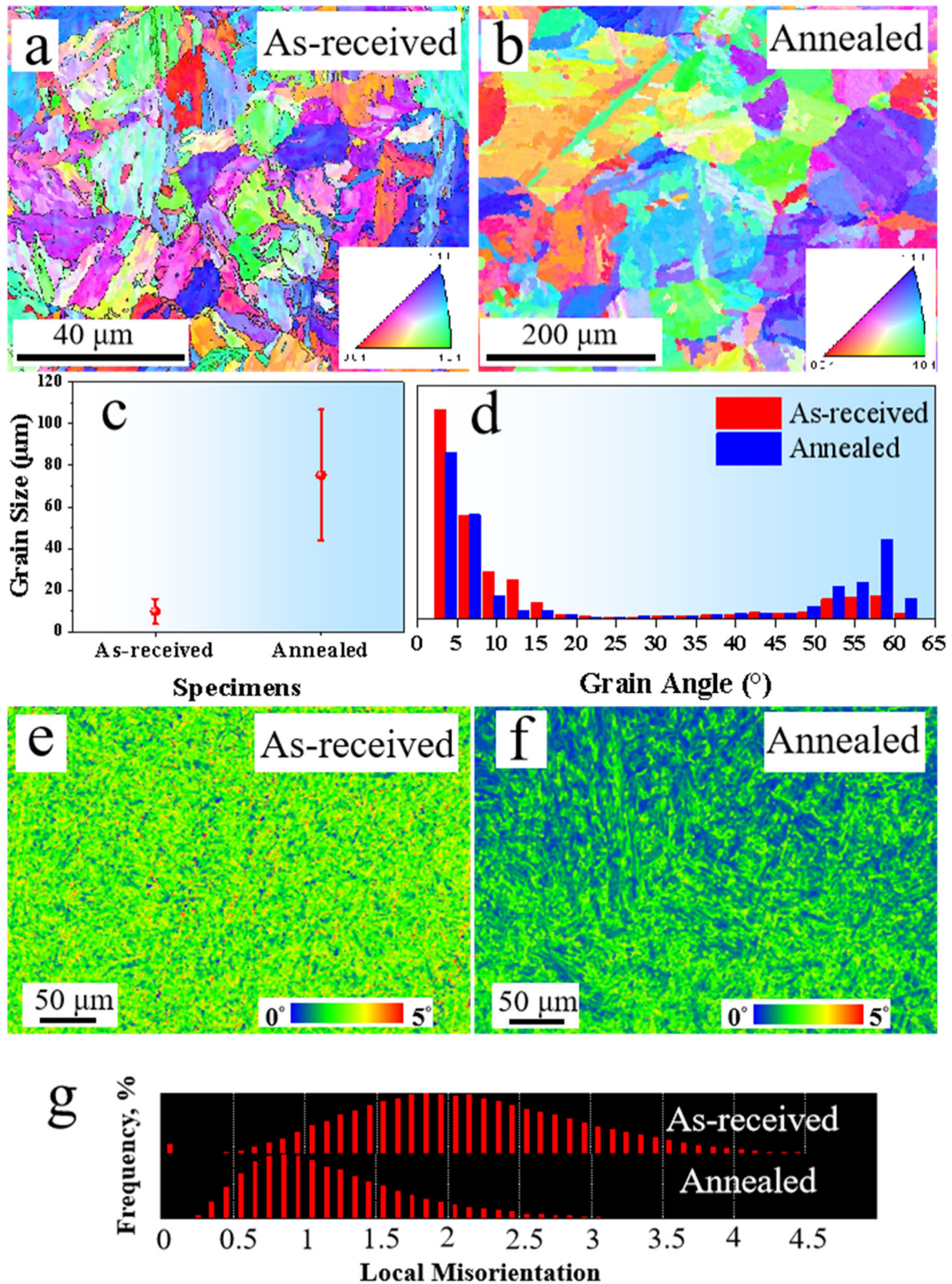


Fig. 2 Inverse pole figure, grain orientation, and kernel average misorientation map comparisons. **a**, **b** Inverse pole figures, **c** grain size distribution, **d** misorientation angle distribution, **e**, **f** color-coded mapping of kernel average misorientation, and **g** the local misorientation distribution of the as-received and annealed E690 steel.

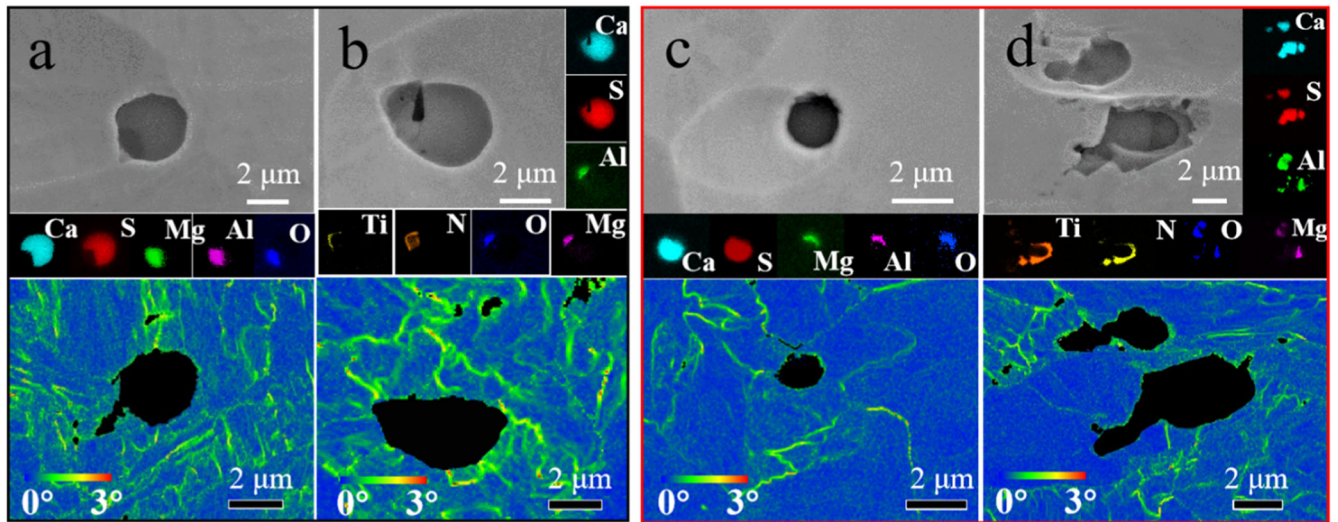


Fig. 3 Secondary electron microscopy images, EDS mapping and EBSD results. **a, c** $\text{CaS-xMgO-yAl}_2\text{O}_3$ inclusions and **(b, d)** $\text{CaS-xMgO-yAl}_2\text{O}_3\text{-TiN}$ inclusions. **a, b** As-received specimen **c, d** annealed specimen.

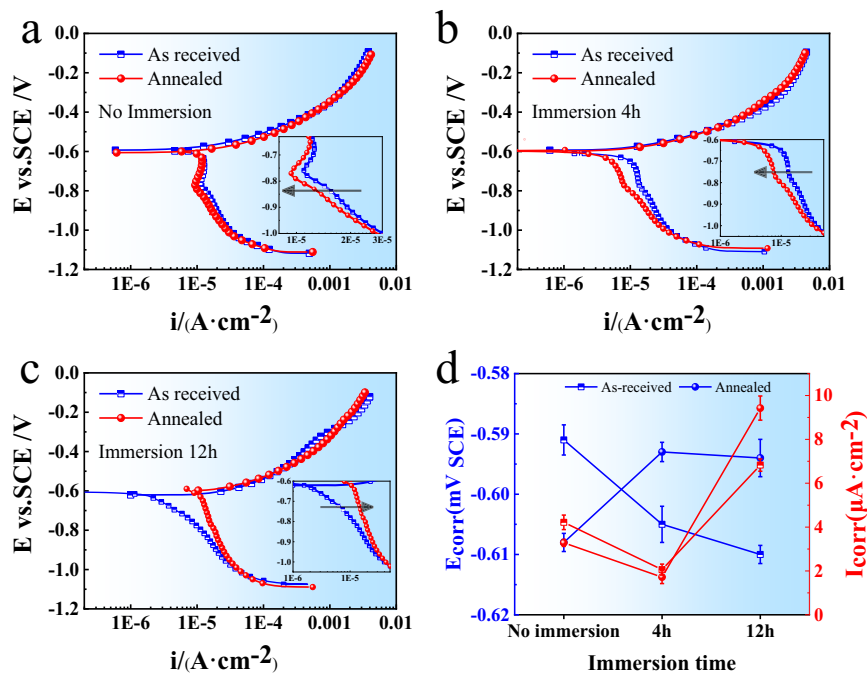


Fig. 4 Polarization curves of as-received and annealed specimens after different immersion times. **a** No immersion, **b** immersion 4 h, **c** immersion 12 h; and **d** $E_{\text{corr}} / I_{\text{corr}}$ of different steels with immersion different time.

All inclusions were spherical or ellipsoidal in shape. No obvious microcrevices (which are considered to promote localized corrosion^{9,12}) were detected on the inclusions or the steel surface.

The KAM represents the degree of local lattice rotation and quantitatively measures the local plastic deformation around the inclusions⁴⁴. In both types of steel, the matrix adjacent to different types of inclusions showed lattice distortion (Fig. 3). The reason is that the irreversible movement of dislocations led to their accumulation at the inclusions/matrix interface⁴⁵. However, compared with Al_2O_3 inclusions examined in a previous study⁹, the dislocation density was lower here due to the soften effect of CaS ⁴⁶. In the current case, the dislocation density around inclusions was higher in the as-received specimen than the annealed one because of dislocation accumulation on the bainite lath boundaries and the grain boundary. Areas with a high

dislocation density always have higher electrochemical activity in the corrosion process⁴⁷, and so they would be easily attacked in the aggressive environment would be easily attacked in the aggressive environment⁴⁸. After heat treatment, the number of dislocation around inclusions obviously decreased. Hence, it could be deduced that when placed in the same corrosion environment, more of the matrix adjacent to inclusions would be dissolved in the as-received specimen, which has a larger area with high lattice distortion than the annealed one.

Electrochemical analysis

The polarization curves of specimens after different immersion times are presented in Fig. 4a–c. The similar anodic curve shapes of two different E690 steels with different immersion time

implying that their anodic electrochemical mechanism remained unchanged after the heat treatment. The active dissolution of iron primarily controlled the anodic reaction⁴⁹. Conversely, the noticeable shift and shape alteration of the cathodic curve shape (Fig. 4a–c) indicates the cathodic reaction was either inhibited or enhanced. Both experimental E690 steels without immersion demonstrated a significant characteristic of oxygen reduction and hydrogen evolution reactions (Fig. 4a)⁴⁹. The cathodic curves of the annealed E690 steel exhibit a left shift compared to the as-received E690 steel, implying the inhibition of the cathodic reaction, as shown in Fig. 4a and b. Which indicated the oxygen reduction that the oxygen uptake reaction of the cathode is inhibited⁵⁰. However, as the immersion time increased to 12 h, the cathodic curves of the annealed E690 steel showed a pronounced right shift compared to the as-received E690 steel (Fig. 4c). This implies that the cathodic reaction of the annealed E690 steel was strengthened.

Fitting results for the corrosion potential and corrosion current are displayed in Fig. 4d. The corrosion potential (E_{corr}) of the as-received specimen decreased along the immersion time increased. The annealed specimens showed the opposite trend. The as-received specimen exhibited a higher corrosion current (I_{corr}) than the annealed specimen. With immersion time increased to 4 h, both of these two specimens exhibit extremely similar I_{corr} . The I_{corr} increased obviously of these two experimental steels along the immersion time increased to 12 h. And the annealed specimen has a distinct higher value than the as-received one, indicating that the former has worse corrosion resistance than the latter.

EIS measurements were performed on the two specimens after they were immersed in the simulated solution for varying durations. Nyquist curves are shown in Fig. 5a and b. After 0–4 h of immersion, inductance tails were observed in the low frequency region of the Nyquist curves. In general, the inductive loop in the low frequency range is caused by the relaxation process of the adsorbed ions, like $(\text{SO}_4^{2-})_{\text{ads}}$ and $(\text{H}^+)_{\text{ads}}$ in the corrosive medium^{51,52}. The appearance of the inductive loop implies the film formed on the specimen surface is not dense or the instability and inadequate cover of rust layer on these two specimens in the early stage of corrosion. When the immersion time was longer than 4 h, the Nyquist curves of both specimens are mainly made of a capacitive arc. The disappearance of inductive loop indicates that the corrosion inhibition effect of the film formed on the specimen surface begins to appear⁵³. The radius of the capacitive arc also increases with the immersion time, indicating that dissolution of metal matrix is restrained to a certain extent by the formation of corrosion product⁵⁴. According to the Bode atlas, the maximum phase angle after 12 h immersion shifts from the medium to the lower frequency regions due to the formation of stable corrosion products^{55,56}. In all curves, the modulus of the maximum phase angle is much lower than 90° , which may be attributed to deviations from ideal capacitor behavior due to local inhomogeneities in the dielectric material, porosity, mass transport, and relaxation effects⁵⁷. Based on the above analysis, two equivalent electric circuits (EECs) were proposed to fit the EIS curves of specimens after different immersion times (Fig. 5e, f). The EEC model contains the following elements: R_s is the solution resistance from the tip of Luggin capillary to the specimen surface, Q_{dl} is capacitance of the electrical double layer, R_{ct} is the charge transfer resistance, R_L and L are the inductance resistance and the inductance related to absorption processes on the interface, Q_f is the capacitance of the surface product layer, and R_f is the resistance of the surface product layer. The fitting results of EIS curves are listed in Table 1. The small chi-square (χ^2) values indicate good agreement between the measured data and the models.

Considering the interaction between different electrical elements in the fitting process, a polarization resistance (R_p) was

proposed to reflect the variation of corrosion resistance during the immersion test. When there is an inductance in the EIS spectra, R_p is calculated according to Eq. (1), while it is calculated according to Eq. (2) in the absence of inductance:

$$\frac{1}{R_p} = \frac{1}{R_{\text{ct}}} + \frac{1}{R_L} \quad (1)$$

$$R_p = R_{\text{ct}} + R_f \quad (2)$$

The relationship between R_p and immersion time is illustrated in Fig. 5g. Before immersion (0 h), the as-received specimen exhibited a lower R_p compared with the annealed one, indicating a higher electrochemical activity in the former. This finding is consistent with the higher dislocation density (Fig. 2e) and lattice distortion density (Fig. 3a, b) in the as-received specimen. After 4 h immersion, both specimens displayed similar and lower R_p . However, when the immersion time exceeded 12 h, R_p increased significantly due to the formation of corrosion rust, indicating an improvement in the barrier properties of the rust during immersion. As shown in Fig. 5g, the as-received specimen has a higher R_p than the annealed one, suggesting that the former has better corrosion resistance.

Analysis of corrosion morphology

In order to track the corrosion initiation and propagation processes, a series of immersion tests were conducted with different durations (1 min, 2 min, 5 min, 30 min, and 12 h). The morphology of localized corrosion on the two specimens after 1 and 2 min are shown in Fig. 6. In both specimens, the first pits appeared at the interface between the inclusion and the matrix. The red arrows in Fig. 6a and b indicate irregular pits that recessed into the matrix in both specimens. Because the original inclusions had a spherical or elliptical shape (as shown in Fig. 3), it is easy to confirm that the matrix was preferentially dissolved. Figure 6a₍₂₎, a₍₃₎, b₍₃₎ and b₍₄₎ show that the nearby matrix around the pits had started to dissolve (marked with blue arrows). What is more, the smooth boundary of the pits and the inclusion in the pits suggest that the inclusions had partially dissolved.

Deeper pits surrounded by a corrosion spot were observed on the as-received (Fig. 6c) and annealed (Fig. 6d) specimens after immersion for 2 min. Residual inclusions at the bottom of the deeper pits and the EDS result confirmed that the CaS part of the inclusions dissolved in such a short time (up to 2 min). It has been reported that CaS is thermodynamically unstable in aqueous solution at room temperature¹². Therefore, these results proved that the CaS part of complex Al-Ca-O-S inclusions in low alloy steel could be dissolved readily in the aqueous solution. MgO·Al₂O₃ would be retained during the localized corrosion initiation process due to their high thermodynamic stability (Fig. 6c, d).

Dissolution of the distorted matrix left microcrevices between the inclusion and the adjacent matrix. Because of the limited mass transport inside the crevices, cations could accumulate and hydrolyze within the crevices to lower the local pH. As the corrosion process progressed, the polarization effect increased, and a more aggressive acidic environment containing Cl⁻, H⁺, and HS⁻ would enhance the dissolution of CaS^{11,20}. Indeed, aggressive anions such as Cl⁻ accumulated by electromigration to maintain charge neutrality in the crevice solution. The cation hydrolysis process would be further strengthened⁴⁸, resulting in an even lower pH and triggering the onset of rapid dissolution of inclusions. This may initiate the dissolution of MgO·Al₂O₃ inclusions, even though MgO·Al₂O₃ could not dissolve easily in the corrosion initiation stage.

The heat treatment would not affect the above-mentioned mechanism of localized corrosion induced by inclusions. In the vicinity of the inclusion, a larger circular corrosion spot was formed around the pit, exhibiting a different morphology from

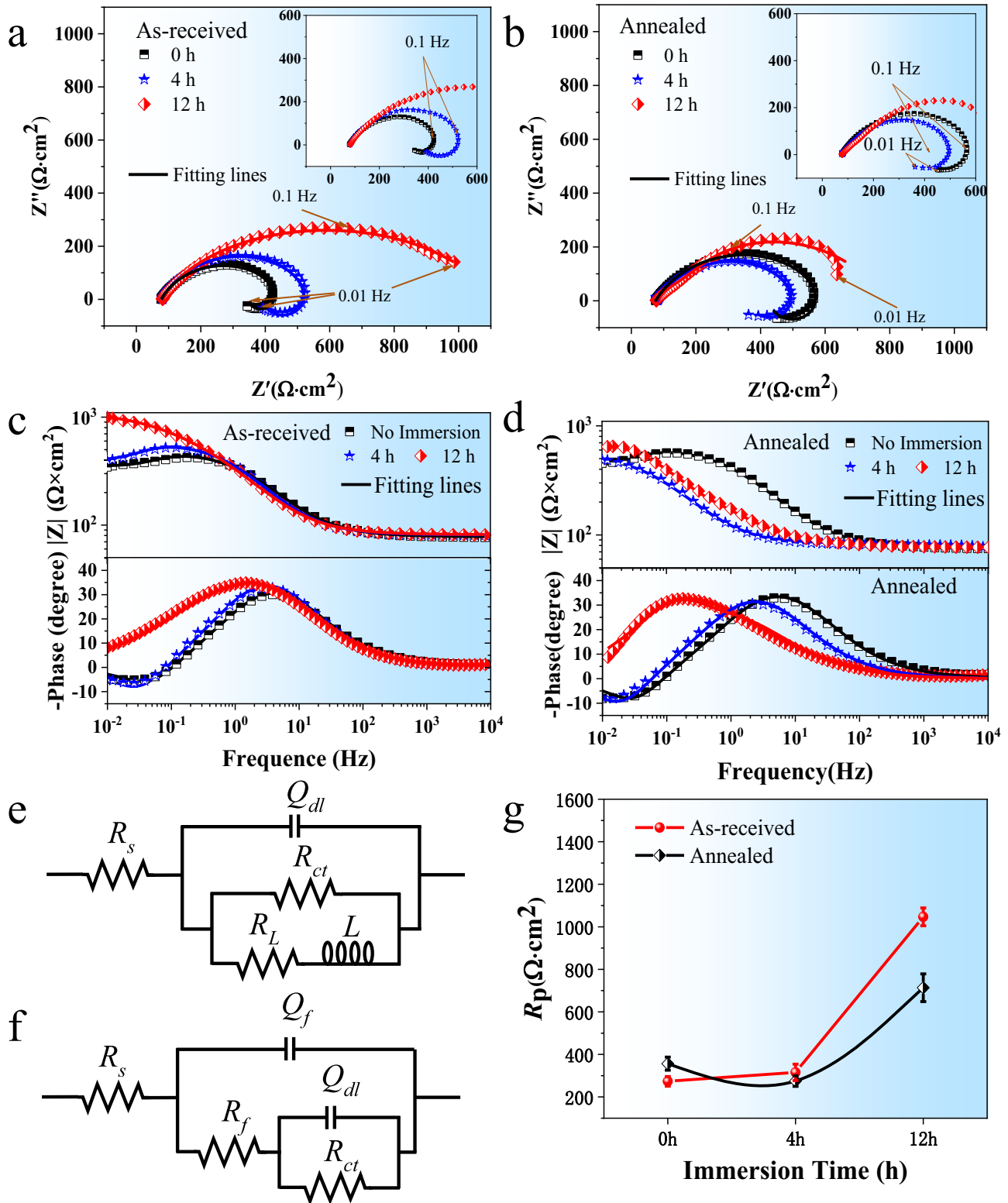


Fig. 5 EIS data of the two experimental steels. **a, c** As-received and **(b, d)** annealed specimens after different immersion times in the simulated solution. **a, b** Nyquist spectra, **c, d** Bode atlas. The equivalent circuit for EIS **(e)** **(f)**, The R_p of as-received and annealed specimens after different immersion times **(g)**.

that of the steel matrix away from the inclusion in both specimens. In the as-received specimen, a mass of nano-scaled carbides were evenly scattered in the formed corrosion spot (Fig. 6c, d). The carbides accelerated the corrosion process due to their higher

Volta potential than the matrix, as proved in our previous research⁵⁸. The nano-scaled precipitates could easily fall off the matrix after the ferrite dissolved. The obvious difference of the secondary phases in the corrosion spot of the as-received

C	Si	Mn	P	S	Cr	Ni	Cu	Al	Ti	Mo	V	Ca	Fe
0.114	0.203	1.056	0.0076	0.002	0.462	1.185	0.016	0.038	0.011	0.484	0.033	0.0017	Bal.

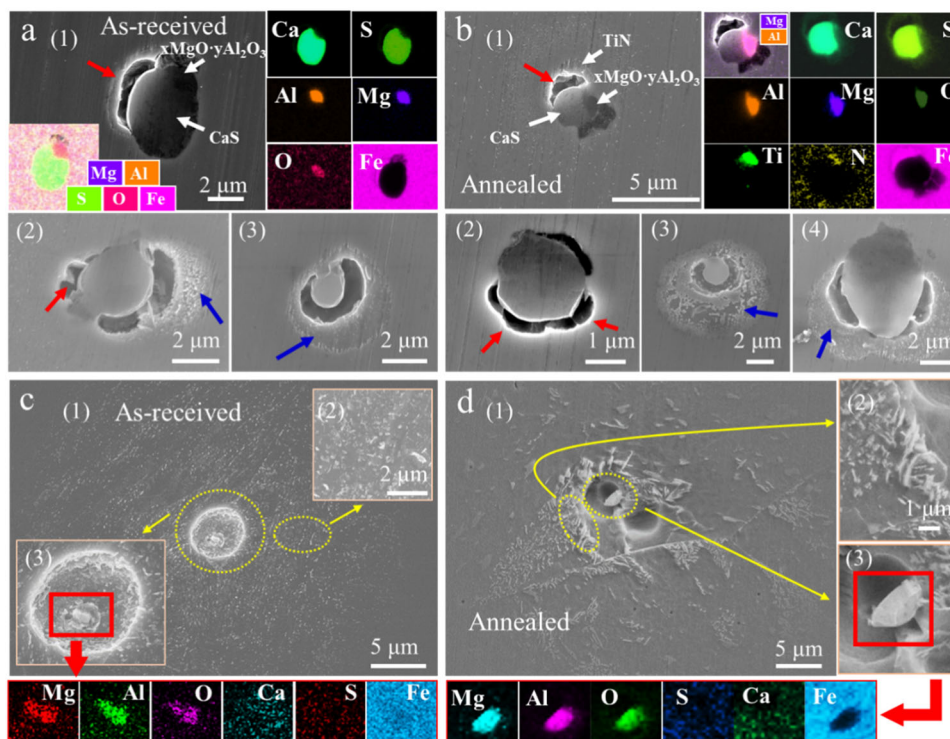


Fig. 6 Localized corrosion morphology and EDS mapping on the experimental steels. **a, c** As-received and **b, d** annealed specimens after immersion for **(a, b)** 1 min and **(c, d)** 2 min.

specimen is that they have larger sizes and are distributed in a relatively concentrated fashion. These larger-sized carbides could be stably retained in the matrix during the corrosion process.

Figure 7 shows the localized corrosion morphology on the as-received and annealed steel after immersion for 5 and 30 min. After 5 min, the two specimens exhibited different corrosion behaviors. In Fig. 7a, several localized pits or corrosion spots were formed. Abundant nanoscale precipitates could be seen in the corrosion spot (Fig. 7a₍₁₎). Higher-resolution images of the pits are shown in Fig. 7a₍₂₎–a₍₄₎. At the center of corrosion spots, there were pits formed after the inclusions have dissolved (Fig. 7a₍₂₎). A single pit without surrounding corrosion spot was observed in Fig. 7a₍₃₎. This also confirms that inclusion dissolution occurred preferentially inside the corrosion spots. These aggressive ions formed in the inclusion dissolution process would diffuse out of the pits evenly in all directions, affecting a ring-shaped area around the pit²⁴. Figure 7a₍₄₎ displays a corrosion spot without a pit formed after dissolution of the inclusion inside. There are two possible routes to form such a corrosion spot. (1) Originally, there were pits caused by the dissolution of smaller inclusions, but they disappeared as the steel matrix was dissolved. (2) Some matrix locations happened to have a higher dislocation density, and localized corrosion was preferentially initiated there²⁹. It was reported that when a dislocation core intersects the exposed metal surface, metal atoms in the adjacent matrix have higher free energy than atoms distant from it, and the former atoms are at a high risk of preferential localized corrosion^{29,59,60}.

Figure 7b displays corrosion morphology on the annealed specimens after immersion for 5 min. Only several smaller

corrosion spots were observed. Figure 7b₍₁₎–b₍₄₎ is higher resolution images of the pits marked in Fig. 7b. Pits with fully or partially dissolved inclusions appeared at the center of the corrosion spot (Fig. 7b₍₁₎ and b₍₂₎). In the corrosion spots, coarse carbides surrounded the pits in the corrosion spots (Fig. 7b₍₃₎ and b₍₄₎). The coarse carbides were larger than those precipitates in the as-received specimen, and their distribution was uneven. Continuously distributed carbides inside the corrosion spot could form abundant galvanic couples and promote the initiation of corrosion. This may explain the different corrosion morphologies between the as-received and annealed specimens.

The corrosion morphology on the as-received and annealed specimens after 30 min of immersion are shown in Fig. 7c and d. For the as-received specimen, when the immersion time increased, numerous large or small-sized corrosion spots appeared on the surface (Fig. 7c). Pits formed after the inclusions had dissolved were also observed inside the corrosion spots (Fig. 7c₍₁₎, c₍₃₎, and c₍₄₎). In Fig. 7c₍₄₎, several small corrosion spots formed by inclusion dissolution began to merge into large ones, indicating an evolution process for the corrosion spots. After the matrix surrounding the pit dissolved, the undissolved inclusion might fall off the matrix. Numerous nanoscale precipitates were observed inside the corrosion spot in Fig. 7c₍₅₎.

The annealed specimen also displayed abundant corrosion spots (Fig. 7d), and pits formed after inclusion dissolution existed inside the corrosion spot after 30-min immersion (Fig. 7d₍₁₎ and d₍₂₎). Larger-sized carbides could be observed inside the corrosion spot. Compared to the nanoscale precipitates seen in the as-received specimen, the larger-sized carbides in the annealed

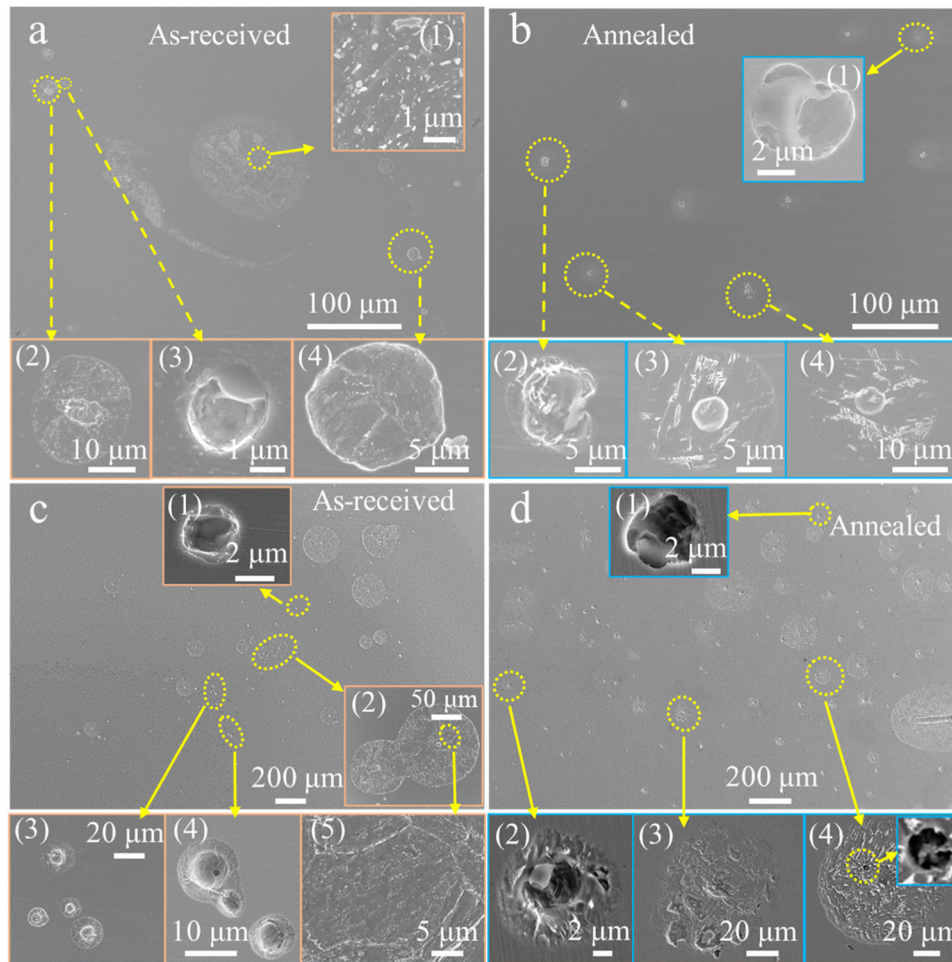


Fig. 7 Localized corrosion morphology and EDS mapping on the experimental steels. **a, c** As-received and **b, d** annealed specimens after immersion for **(a, b)** 5 min and **(c, d)** 30 min.

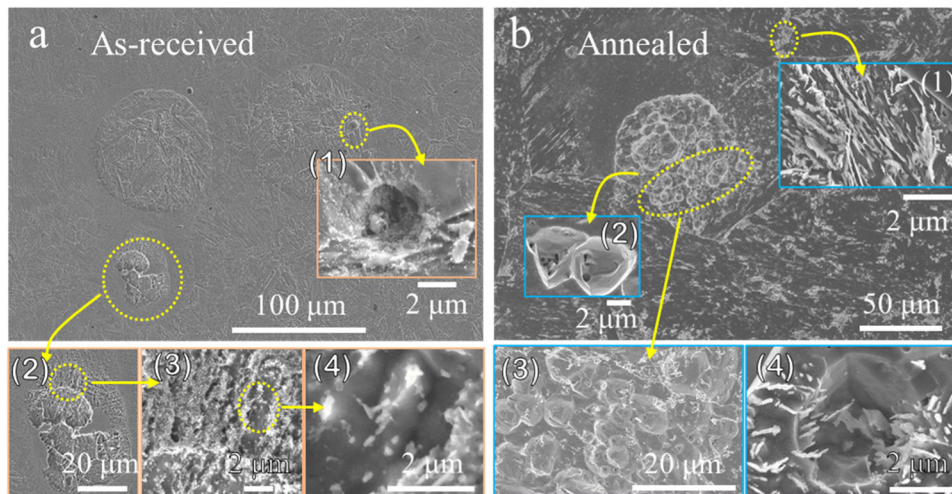


Fig. 8 Corrosion morphology on the experimental steels. **a** As-received and **b** annealed specimens after immersion for 12 h.

specimen were more stably retained during the corrosion process, which would provide a continuous galvanic couple effect during the process of corrosion extension²⁷.

After immersion for 12 h, the matrix in both types of specimens further dissolved (Fig. 8a, b). Pits formed due to inclusion dissolution (Fig. 8a₍₁₎ and b₍₄₎) could be observed on the

specimens. This is inevitable: because inclusions were evenly distributed throughout the steel, new inclusions became exposed on the specimen surface as the matrix continuously dissolved. Figure 8a₍₂₎–a₍₄₎ reveal the propagation of corrosion spots. Figure 8a₍₃₎ shows the boundary of the corrosion spot with a gully morphology, which is due to the dissolution of ferrite under the

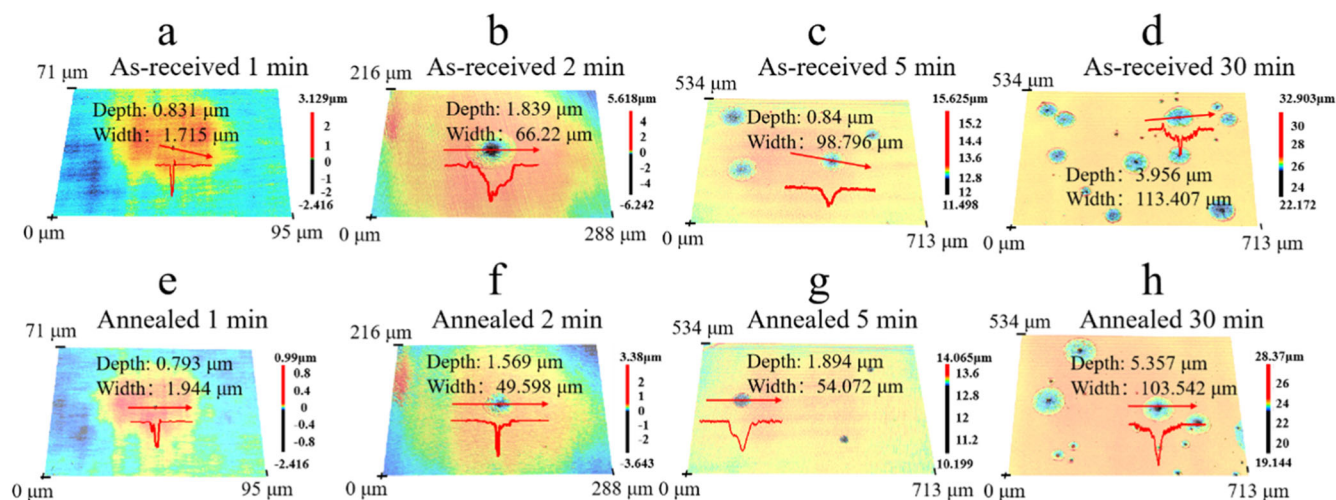


Fig. 9 Surface morphology and 3-dimensional structure of the initial localized corrosion in the experimental steels. **a, c, e, g** As-received and **b, d, f, h** annealed specimens after immersion for **(a, b)** 1 min, **(c, d)** 2 min, **(e, f)** 5 min, and **(g, h)** 30 min.

galvanic couple effect. There were a great amount of nanoscale precipitates inside the corrosion spot in Fig. 8a₍₄₎. After immersion for 12 h, a severely corrosion morphology appeared on the annealed specimen (Fig. 8b). After the ferrite dissolved, strips of carbide were retained on the specimen surface (Fig. 8b₍₁₎), confirming that larger-sized carbides could remain in the matrix. These carbides maintained a continuous galvanic couple effect in the corrosion extension process and accelerated the corrosion reaction⁶¹. Numerous pits induced by the carbides were also observed in the annealed specimen (Fig. 8b₍₂₎) and b₍₃₎). Again, there were larger-sized carbides embedded in the matrix around the pits or intersecting the pits on the surface (Fig. 8b₍₄₎).

Kinetic analysis of the localized corrosion initiation process

In the immersion test, the specimens showed localized corrosion morphology within 30 min. To further examine the initiation of localized corrosion, the typical pitting depth, and 3-D morphology were measured at high magnification (Fig. 9). In both types of specimens, the pits had an open hemispherical cavity, and the diameter of the pitting holes increased with the immersion time. This is different from the case of stainless steel, in which the formed pits have an overall hemispherical or dish shape^{62–64}.

The pit density was also statistically analyzed based on 50 randomly selected visual fields, in order to investigate the rate of localized corrosion initiation between the two types of specimens. The obtained pit densities are displayed in Fig. 10. For both types of specimens, the pit density increased upon extending the immersion time. Intriguingly, the pit density is always slightly higher in the as-received specimen compared to the annealed one. Considering the similar amount and distribution of inclusions in these two specimens, we attribute their difference in pit density to a change in dislocation density. Metal atoms in a matrix with a higher dislocation density will have higher free energy. According to Gutman's mechano-electrochemistry theory⁴⁷, the electrochemical activity would increase due to the lattice distortion. Hence, localized corrosion is preferentially initiated at these locations to relieve the stored energy through the metal/electrolyte interface²⁹.

The ratio of pit depth to pit mouth diameter (k) is typically used to characterize the pit extension process⁶⁵. Normally, there is a liner relationship between the ratio k and the pit volume, as described by following:

$$k = aV + b \quad (3)$$

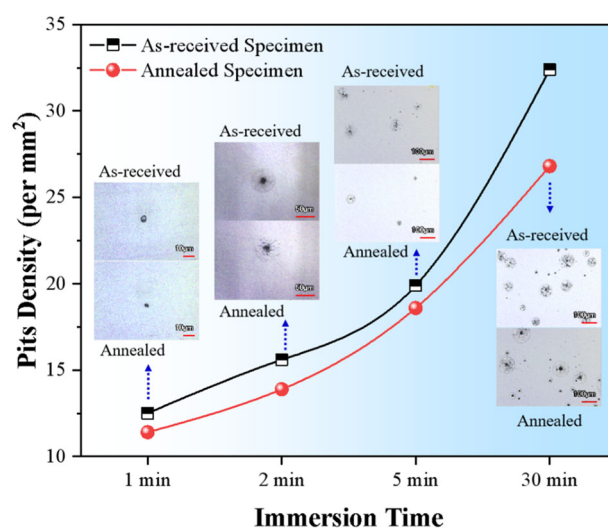


Fig. 10 Statistical analysis of pit characteristics. Pit density on the as-received and annealed specimens after immersion for 1, 2, 5, and 30 min.

where a and b are constants, and V is the pit volume. k decreases as the pit volume increases when $a < 0$, and vice versa. Stainless steel has $a > 0$, meaning that the pits will quickly extend longitudinally and become stabilized⁶⁶. Figure 11 plots k vs. V for the as-received and annealed specimens after different immersion times. All fitting lines show negative slopes that become less steep at longer immersion times. This indicates that the pit mouth diameter increases more rapidly than the pit depth in the early stage of corrosion initiation. The smaller absolute value of k at longer immersion times indicates a declining contribution from pitting corrosion during to the corrosion evolution process. This is also consistent with the uniform corrosion morphology observed after much longer immersion times (such as 12 h).

Mechanism of the corrosion initiation and propagation

According to the analysis above, the localized corrosion was mainly induced by inclusions. Heat treatment did not change this mechanism. First, the area with lattice distortion around the inclusion is dissolved (Fig. 6a, b). The reason is that this area had higher electrochemical activity due to the high local dislocation

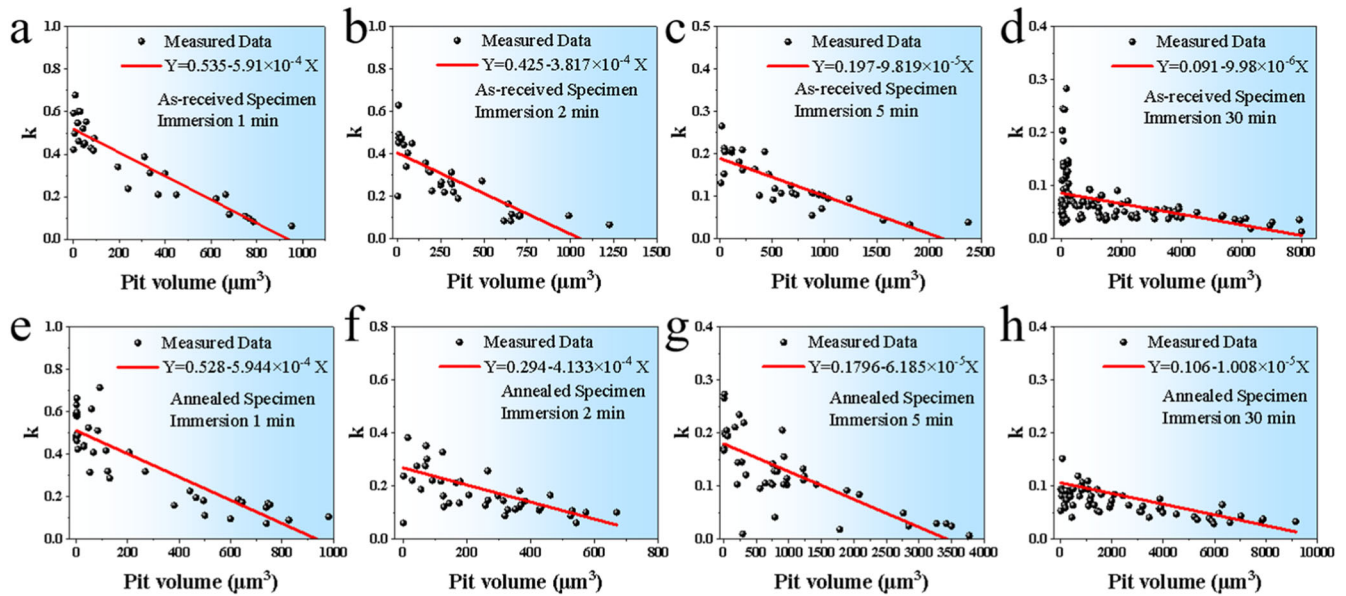


Fig. 11 Ratio of pit depth to mouth diameter (k) of the as-received and annealed specimens after different immersion times. **a** As-received specimen immersion 1 min, **b** as-received specimen immersion 2 min, **c** as-received specimen immersion 5 min, **d** as-received specimen immersion 30 min, **e** annealed specimen immersion 1 min, **f** annealed specimen immersion 2 min, **g** annealed specimen immersion 5 min, and **h** annealed specimen immersion 30 min.

density^{9,21,47}, and therefore it was easily attacked in the aggressive environment⁴⁸. With matrix dissolution in the dislocation region, an oxygen concentration cell would be formed in the micro-pits owing to the oxygen-concentration gradient, accelerating further matrix dissolution. While the CaS portion dissolved in the corrosion process (Fig. 6c, d), an aggressive environment was formed in the pits. To maintain charge balance in the pit with a continuous influx of Cl^- , the matrix had to be hydrolyzed continuously, which resulted in a catalytic occluded cell with the micro-pits acting as anodes⁶⁷. A decreased pH caused the $\text{xMgO}\cdot\text{yAl}_2\text{O}_3$ inclusions to dissolve (Fig. 7). The TiN portion with high thermodynamic stability might fall off the matrix during/after matrix dissolution. In our immersion test results (Fig. 8), both the as-received and annealed specimens exhibited uniform corrosion after a long immersion time (e.g., 12 h).

In the early stage (e.g., the first 30 min), localized corrosion was the main corrosion morphology. Statistical analysis results in Fig. 10 indicate that the pit density was always higher in the as-received specimen than that in the annealed specimen. This presumably results from a difference in dislocation density, because the inclusion conditions were similar between these two types of specimens. When the matrix has a higher dislocation density, metal atoms therein have higher free energy, which causes higher electrochemical activity in the area⁴⁷. Thus, localized corrosion could easily initiate and extend in the area with higher dislocation density. Metal atoms adjacent to a dislocation core that intersects the exposed metal surface also have higher free energy than atoms distant from it, which may indicate that emergent ends of edge/screw dislocations are the preferred sites for corrosion redox reactions^{29,59,60,68}. Hence, localized corrosion is favorably initiated at these locations to relieve stored energy through the metal/electrolyte interface^{21,29,69}. Corrosion spots without inclusion inside them, such as the one shown in Fig. 7a₍₄₎, might lead to the higher pit density observed in the as-received specimen. Kinetic analysis of the localized corrosion initiation process indicated that the weight of pitting corrosion decreased during the corrosion evolution process (Fig. 11). This is also consistent with the uniform corrosion morphology seen after longer immersion times such as 12 h.

After the immersion test, corrosion spots could be observed around inclusions (Figs. 6 and 8). Corrosion spots on the as-received and annealed specimens underwent similar evolution processes, as shown in Fig. 12a–d. Pits would be preferentially formed at the inclusion location. As the corrosion product spread outward from the pit center, obvious corrosion spots could be seen around the inclusion (Fig. 12b). As the immersion time increased, the corrosion spots began to merge (Fig. 12c and d). Figure 12e and f schematically depict the formation and propagation of corrosion spots, respectively. During the initiation of localized corrosion, after the dissolution of the inclusions and their adjacent matrix, the aggressive ions diffused isotropically out of the inclusions, forming a ring-shaped zone around the inclusion with a more corrosive environment than the matrix far away (Fig. 12e). Fe^{2+} ion was formed in this zone, diffused to the matrix further away, and reacted with OH^- to form a rust film there. This caused an oxygen-concentration cell to form between the ring zone and the matrix further away, accelerating dissolution of the ring zone. Further, carbide is normally regarded as the cathodic phase and will accelerate matrix dissolution in the ring zone^{27,70}. All these events led to the formation of corrosion spots during the early stage of corrosion. At longer immersion times, distinct corrosion spots were formed around individual inclusions. As the matrix continuously dissolved, the corrosion spots fused with each other, and the surface displayed uniform corrosion (Fig. 12f).

Heat treatment reduced the dislocation density in the steel (Fig. 2g). As shown in Fig. 4d, the as-received specimen had a larger corrosion current than the annealed one without no immersion, indicating that the former has worse resistance against uniform corrosion. The polarization curves indicated the anodic reaction was mainly controlled by the active dissolution of iron (Fig. 4a–c)⁴⁹. The left shift of the cathodic polarization curves in the annealed E690 steel (Fig. 4a, b) compared with the as-received one in the condition of no immersion and immersion 4 h implied the cathodic reaction was inhibited. This could be result from the lower dislocation density in the annealed specimen, which directly reduced the amount of corrosion active sites in the corrosion initiation early stage^{22,40,48}. Before the immersion test (0 h), the as-received specimen had a lower R_p than the annealed one, indicating its relatively high electrochemical activity owing to a higher density of lattice distortions. After 4 h immersion, both two

specimens had lower R_p , possibly because in this period localized corrosion induced by inclusion dissolution was the main contributor to corrosion. Also, inclusions in these two specimens had similar conditions. When the immersion time increased to 12 h, the cathodic reaction of the annealed specimen was strengthened (Fig. 4c). After 12 h, the R_p of the annealed specimens continued to decrease. The corrosion morphologies shown in Fig. 8b shows that a large amount of pearlite directly leads to the appearance of corrosion pits of large size in the annealed specimen. These findings suggest that the retained austenite contribute to corrosion via microscopic galvanic effects at ferrite-austenite interfaces and promote ferrite dissolution therein²⁶. Additionally, the coarsened carbide would also accelerate the corrosion process²⁷. However, the R_p of as-received specimen increased distinctly with the formation of corrosion rust, indicating an increased barrier effect of rust during immersion. The annealed specimen had a higher R_p than the as-received one and therefore probably better corrosion resistance.

The influence of heat treatment on the corrosion resistance of materials is a complex phenomenon. This study aims to analyze the mechanism of corrosion resistance evolution in materials by

examining microstructural changes. Our findings suggest that the initiation mechanism of localized corrosion is not affected by heat treatment, as it is primarily caused by the dissolution of inclusions or the adjacent matrix. During the early stages of corrosion, both the as-received and annealed specimens show dominant localized corrosion. However, its contribution decreases as corrosion progresses with increasing immersion time.

METHODS

Materials and methods

E690 steel was processed by Nanjing Iron and Steel Group using thermal mechanical control processing. Its chemical composition is given in Table 2.

For the heat treatment, the specimen was heated to 1200 °C for 30 min, and then cooled in the furnace. Samples with a size of 10 mm × 10 mm × 6 mm were mechanically ground and polished. Then, they were cleaned ultrasonically in ethanol and dried in cool air. To prevent the mechanical polishing process from interfering with microstructural observation, these samples were manually ground to 30 μm with silicon-carbide paper and then reduced

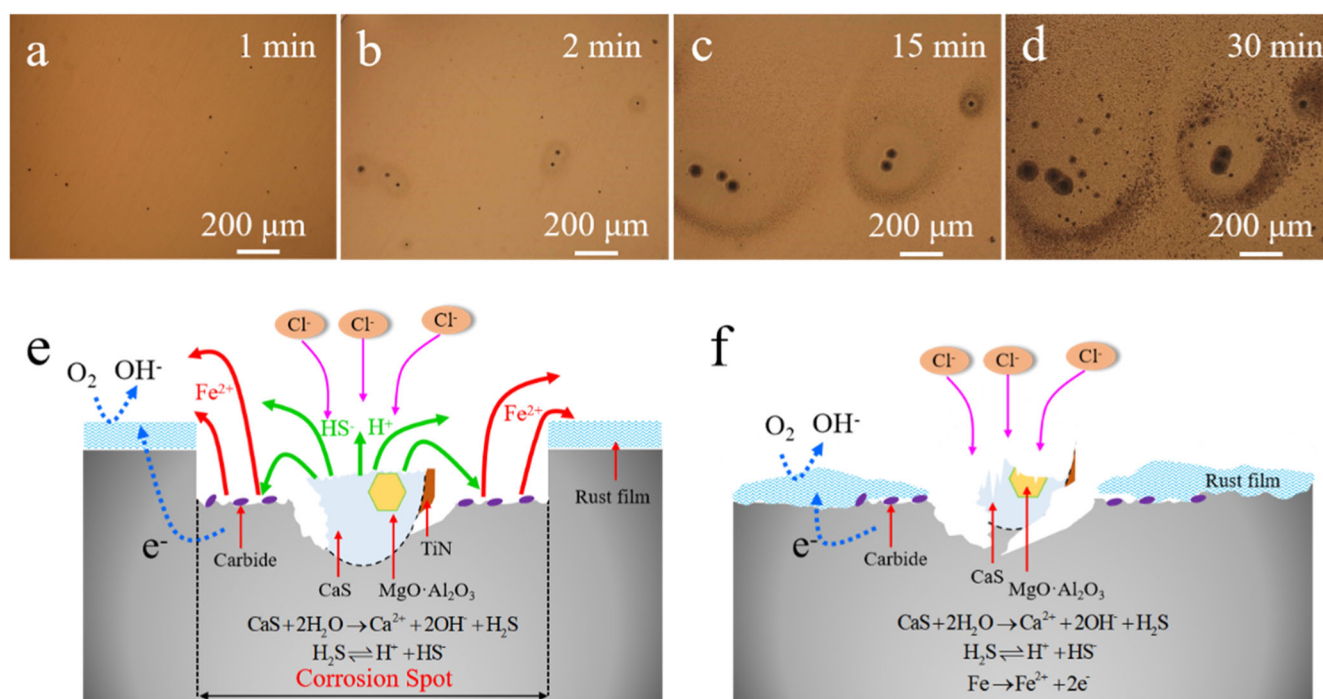


Fig. 12 Corrosion morphology evolution tracing and corrosion mechanism model. **a–d** Evolution of corrosion spots formed on the as-received specimens. Schematic representation of reactions during the **(e)** formation and **(f)** propagation of corrosion spots.

Table 2. Fitting results of EIS curves for the as-received and annealed specimens (denoted as AR and AN, respectively) after different immersion times.

	Time h	R_s Ω -cm ²	$Q_f \times 10^{-4}$ Ω^{-1} cm ⁻² s ⁿ	n_f	$Q_{dl} \times 10^{-4}$ Ω^{-1} cm ⁻² s ⁿ	n_{dl}	R_f Ω -cm ²	R_{ct} Ω -cm ²	R_L Ω -cm ²	L H-cm ⁻²	$\chi^2 \times 10^{-4}$
AR	0	77.16			4.970	0.73		393.4	896.5	2977	2.923
	4	80.31			5.710	0.748		488.9	890.6	5464	2.589
	12	80.78	7.258	0.715	25.67	0.549	554.6	482.2			2.307
AN	0	75.24			4.360	0.707		550.5	101.2	6344.0	3.085
	4	80.87			7.844	0.723		457.9	686.4	7271.0	7.006
	12	77.75	2.188	0.656	25.69	0.991	331.9	381.8			0.619

with argon ions (Gatan 691 Precision Ion Polishing System). For the EBSD test, specimens were mechanically polished and then electropolished in an electrolyte of 10 vol.% perchloric acid in ethanol. Samples used for the TEM test were ground down to 2000 grit, polished to a thickness of 30 μm , and then further polished by ion beam in the same system mentioned above, until the center of the sample was perforated.

Microstructural characterization

The morphology and composition of inclusions were characterized by FE-SEM (Zeiss Merlin, Germany) and EDS on ion-polished samples, so that the mechanical polishing process would not affect the characterization⁹. For microstructural observation, the samples were etched with 4% Nital solution and then observed with FE-SEM. TSL data acquisition software integrated with the FE-SEM system was used to capture the EBSD data. The nanoscale structure was characterized by TEM (JEOL JSM-7100F, Japan).

Electrochemical measurements

The electrochemical measurements were performed with a potentiostat (VersaStudio 3F; Princeton, USA). Electrochemical polarization and EIS were performed in a three-electrode set-up using the steel electrode, a platinum sheet electrode, and saturated calomel electrode (SCE) as the working electrode, counter electrode, and reference electrode, respectively. The samples were sealed in epoxy resin except for a 10 mm \times 10 mm surface. The open circuit potential (OCP) was monitored for 3600 s to obtain an electrochemical steady state. After different immersion times (0–12 h), EIS measurements were conducted in the frequency range from 10^4 to 10^{-2} Hz. A sinusoidal perturbation of 10 mV (peak-to-peak value) was imposed at open circuit potential over the frequency during the EIS test. with a dynamic potential polarization curve scanning rate of 10 mV/min after immersion different times. The potentiodynamic polarization curves were conducted from OCP to the anodic and cathodic directions, respectively, with a scan rate of 10 mV/min. The aqueous solution used for immersion had a pH = 4.9 and contained 0.1 wt.% NaCl, 0.05 wt.% Na_2SO_4 , and 0.05 wt.% CaCl_2 ⁷¹, in order to simulate thin liquid films formed under a humid marine environment at Xisha Islands in the South China Sea. The solution used in this work is an aerated solution.

Immersion test

FE-SEM-EDS was used to observe the corrosion morphology of immersed specimens, including the initiation of localized corrosion and the transition to uniform corrosion. After the specimens were immersed for 1 min, 2 min, 5 min, 30 min, and 12 h, the rust on their surface was removed using a solution containing 50% HCl, 50% deionized water, and 5–8 g/L $\text{C}_6\text{H}_{12}\text{N}_4$. The morphology of localized corrosion formed in the early stage was examined under a laser confocal microscope (VKX250; Keyence, Japan) with a motorized Z-axis stage. All tests were conducted at ambient temperature. The reported results are the average of three repeated measurements. In this study, we utilized FE-SEM to collect a minimum of 20 random fields of view for observing the corrosion morphology of the material under each condition. The resulting corrosion patterns were subjected to statistical analysis.

DATA AVAILABILITY

The relevant data is available from the corresponding author upon reasonable request.

Received: 8 October 2022; Accepted: 3 May 2023;
Published online: 24 May 2023

REFERENCES

1. Tianliang, Z., Zhiyong, L., Cuiwei, D., Chunduo, D., Xiaogang, L. & Bowei, Z. Corrosion fatigue crack initiation and initial propagation mechanism of E690 steel in simulated seawater. *Mater. Sci. Eng. A* **708**, 181–192 (2017).
2. Liu, Z. Y., Hao, W. K., Wu, W., Luo, H. & Li, X. G. Fundamental investigation of stress corrosion cracking of E690 steel in simulated marine thin electrolyte layer. *Corros. Sci.* **148**, 388–396 (2019).
3. Li, Y., Liu, Z., Wu, W., Li, X. & Zhao, J. Crack growth behaviour of E690 steel in artificial seawater with various pH values. *Corros. Sci.* **164**, 108336 (2020).
4. Li, X., Zhang, D., Liu, Z., Li, Z., Du, C. & Dong, C. Materials science: Share corrosion data. *Nature* **527**, 441–442 (2015).
5. Ma, H. et al. Comparative study on corrosion fatigue behaviour of high strength low alloy steel and simulated HAZ microstructures in a simulated marine atmosphere. *Int. J. Fatigue* **137**, 105666 (2020).
6. Wu, W., Liu, Z., Li, X., Du, C. & Cui, Z. Influence of different heat-affected zone microstructures on the stress corrosion behavior and mechanism of high-strength low-alloy steel in a sulfured marine atmosphere. *Mater. Sci. Eng. A* **759**, 124–141 (2019).
7. Park, H., Park, C., Lee, J., Kang, N. & Liu, S. Influence of hydrogen on softened heat-affected zones during in-situ slow strain rate testing in advanced high-strength steel welds. *Corros. Sci.* **181**, 109229 (2021).
8. Liu, C. et al. Influence of rare earth metals on mechanisms of localised corrosion induced by inclusions in Zr-Ti deoxidised low alloy steel. *Corros. Sci.* **166**, 108463 (2020).
9. Liu, C. et al. Role of Al_2O_3 inclusions on the localized corrosion of Q460NH weathering steel in marine environment. *Corros. Sci.* **138**, 96–104 (2018).
10. Li, G., Wang, L., Wu, H., Liu, C., Wang, X. & Cui, Z. Dissolution kinetics of the sulfide-oxide complex inclusion and resulting localized corrosion mechanism of X70 steel in deaerated acidic environment. *Corros. Sci.* **174**, 108815 (2020).
11. Liu, C. et al. Towards a better understanding of localised corrosion induced by typical non-metallic inclusions in low-alloy steels. *Corros. Sci.* **179**, 109150 (2021).
12. Wang, L. et al. Influence of inclusions on initiation of pitting corrosion and stress corrosion cracking of X70 steel in near-neutral pH environment. *Corros. Sci.* **147**, 108–127 (2019).
13. Yang, Z., Kan, B., Li, J., Su, Y., Qiao, L. & Volinsky, A. A. Pitting initiation and propagation of x70 pipeline steel exposed to chloride-containing environments. *Materials* **10**, 1076 (2017).
14. Jin, T. Y. & Cheng, Y. F. In situ characterization by localized electrochemical impedance spectroscopy of the electrochemical activity of microscopic inclusions in an X100 steel. *Corros. Sci.* **53**, 850–853 (2011).
15. Park, I.-J., Lee, S.-M., Kang, M., Lee, S. & Lee, Y.-K. Pitting corrosion behavior in advanced high strength steels. *J. Alloy. Compd.* **619**, 205–210 (2015).
16. Xue, W. et al. Initial microzonal corrosion mechanism of inclusions associated with the precipitated (Ti, Nb)N phase of Sb-containing weathering steel. *Corros. Sci.* **163**, 108232 (2020).
17. Su, H., Wei, S., Liang, Y., Wang, Y., Wang, B. & Yuan, Y. Pitting behaviors of low-alloy high strength steel in neutral 3.5 wt% NaCl solution based on in situ observations. *J. Electroanal. Chem.* **863**, 114056 (2020).
18. Zheng, S. J. et al. Identification of MnCr_2O_4 nano-octahedron in catalysing pitting corrosion of austenitic stainless steels. *Acta Mater.* **58**, 5070–5085 (2010).
19. Hou, Y., Li, T., Li, G. & Cheng, C. Mechanism of Yttrium composite inclusions on the localized corrosion of pipeline steels in NaCl solution. *Micron* **130**, 102820 (2020).
20. Liu, C., Revilla, R. I., Liu, Z., Zhang, D., Li, X. & Terry, H. Effect of inclusions modified by rare earth elements (Ce, La) on localized marine corrosion in Q460NH weathering steel. *Corros. Sci.* **129**, 82–90 (2017).
21. Kong, D. et al. Mechanical properties and corrosion behavior of selective laser melted 316L stainless steel after different heat treatment processes. *J. Mater. Sci. Technol.* **35**, 1499–1507 (2019).
22. Yang, Y., Zhang, T., Shao, Y., Meng, G. & Wang, F. New understanding of the effect of hydrostatic pressure on the corrosion of Ni–Cr–Mo–V high strength steel. *Corros. Sci.* **73**, 250–261 (2013).
23. Liu, C. et al. Synergistic effect of Al_2O_3 inclusion and pearlite on the localized corrosion evolution process of carbon steel in marine environment. *Materials* **11**, 2277 (2018).
24. Wang, S. et al. Effect of H_3BO_3 on corrosion in 0.01M NaCl solution of the interface between low alloy steel A508 and alloy 52M. *Corros. Sci.* **102**, 469–483 (2016).
25. Tewary, N. K., Kundu, A., Nandi, R., Saha, J. K. & Ghosh, S. K. Microstructural characterisation and corrosion performance of old railway girder bridge steel and modern weathering structural steel. *Corros. Sci.* **113**, 57–63 (2016).
26. Guo, L. Q., Li, M., Shi, X. L., Yan, Y., Li, X. Y. & Qiao, L. J. Effect of annealing temperature on the corrosion behavior of duplex stainless steel studied by in situ techniques. *Corros. Sci.* **53**, 3733–3741 (2011).

27. Liu, C., Zhao, J., Li, X., Yang, J., Ma, H. & Li, X. Size dependency between the carbides and durability of X80 steel in acid solid environment. *J. Electroanal. Chem.* **873**, 114506 (2020).
28. Marco, D. C. B. K. P. R. D. The influence of microstructure on the corrosion rate of various carbon steels. *J. Appl. Electrochem.* **35**, 139–141 (2005).
29. Escrivà-Cerdán, C., Ooi, S. W., Joshi, G. R., Morana, R., Bhadeshia, H. K. D. H. & Akid, R. Effect of tempering heat treatment on the CO₂ corrosion resistance of quenched-hardened Cr-Mo low-alloy steels for oil and gas applications. *Corros. Sci.* **154**, 36–48 (2019).
30. Ma, H., Liu, Z., Du, C., Li, X. & Cui, Z. Comparative study of the SCC behavior of E690 steel and simulated HAZ microstructures in a SO₂-polluted marine atmosphere. *Mater. Sci. Eng. A* **650**, 93–101 (2016).
31. Tian, H. et al. Electrochemical corrosion, hydrogen permeation and stress corrosion cracking behavior of E690 steel in thiosulfate-containing artificial seawater. *Corros. Sci.* **144**, 145–162 (2018).
32. Kong, D. et al. The passivity of selective laser melted 316L stainless steel. *Appl. Surf. Sci.* **504**, 144495 (2020).
33. Arafin, M. A. & Szpunar, J. A. A new understanding of intergranular stress corrosion cracking resistance of pipeline steel through grain boundary character and crystallographic texture studies. *Corros. Sci.* **51**, 119–128 (2009).
34. Lu, J. & Szpunar, J. A. Microstructural model of intergranular fracture during tensile tests. *J. Mater. Process. Technol.* **60**, 305–310 (1996).
35. Liu, Z., Hou, Q., Li, C., Li, X. & Shao, J. Correlation between grain boundaries, carbides and stress corrosion cracking of Alloy 690TT in a high temperature caustic solution with lead. *Corros. Sci.* **144**, 97–106 (2018).
36. Eskandari, M., Mohtadi-Bonab, M. A. & Szpunar, J. A. Evolution of the microstructure and texture of X70 pipeline steel during cold-rolling and annealing treatments. *Mater. Des.* **90**, 618–627 (2016).
37. Bhadeshia, H. & Honeycombe, R. *Steels: microstructure and properties*. (Butterworth-Heinemann, 2017).
38. Ooi, S., Ramjaun, T., Hulme-Smith, C., Morana, R., Drakopoulos, M. & Bhadeshia, H. Designing steel to resist hydrogen embrittlement Part 2—precipitate characterisation. *Mater. Sci. Technol.* **34**, 1747–1758 (2018).
39. Liu, C. et al. New insights into the mechanism of localised corrosion induced by TiN-containing inclusions in high strength low alloy steel. *J. Mater. Sci. Technol.* **124**, 141–149 (2022).
40. Zhang, T. et al. Integral effects of Ca and Sb on the corrosion resistance for the high strength low alloy steel in the tropical marine environment. *Corros. Sci.* **208**, 110708 (2022).
41. Park, J. H., Lee, S.-B. & Kim, D. S. Inclusion control of ferritic stainless steel by aluminum deoxidation and calcium treatment. *Metall. Mater. Trans. B.* **36**, 67–73 (2005).
42. Liu, J.-H., Wu, H.-J., Bao, Y.-P. & Wang, M. Inclusion variations and calcium treatment optimization in pipeline steel production. *Int. J. Miner. Metall. Mater.* **18**, 527–534 (2011).
43. Yang, S., Wang, Q., Zhang, L., Li, J. & Peaslee, K. Formation and modification of MgO-Al₂O₃-based inclusions in alloy steels. *Metall. Mater. Trans. B.* **43**, 731–750 (2012).
44. Zhao, T., Liu, Z., Chao, L., Dai, C., Du, C. & Li, X. Variation of the corrosion behavior prior to crack initiation of E690 steel fatigued in simulated seawater with various cyclic stress levels. *J. Mater. Eng. Perform.* **27**, 4921–4931 (2018).
45. Tanaka, K. & Mura, T. A theory of fatigue crack initiation at inclusions. *Metall. Trans. A* **13**, 117–123 (1982).
46. Xu, G., Jiang, Z. & Li, Y. Formation mechanism of CaS-bearing inclusions and the rolling deformation in al-killed, low-alloy steel with Ca treatment. *Metall. Mater. Trans. B* **47**, 2411–2420 (2016).
47. Gutman, E. M. *Mechanochemistry of Solid Surfaces*. (World Scientific Publishing Company, 1994).
48. Guo, X., Gin, S., Lei, P., Yao, T., Liu, H., Schreiber, D. K., Ngo, D., Viswanathan, G., Li, T., Kim, S. H., Vienna, J. D., Ryan, J. V., Du, J., Lian, J. & Frankel, G. S. Self-accelerated corrosion of nuclear waste forms at material interfaces. *Nat. Mater.* **19**, 310–316 (2020).
49. Lu, Q., Wang, L., Xin, J., Tian, H., Wang, X. & Cui, Z. Corrosion evolution and stress corrosion cracking of E690 steel for marine construction in artificial seawater under potentiostatic anodic polarization. *Constr. Build. Mater.* **238**, 117763 (2020).
50. Flitt, H. J. & Schweinsberg, D. P. A guide to polarisation curve interpretation: deconstruction of experimental curves typical of the Fe/H₂O/H⁺/O₂ corrosion system. *Corros. Sci.* **47**, 2125–2156 (2005).
51. Qiang, Y., Zhi, H., Guo, L., Fu, A., Xiang, T. & Jin, Y. Experimental and molecular modelling studies of multi-active tetrazole derivative bearing sulfur linker for protecting steel from corrosion. *J. Mol. Liq.* **351**, 118638 (2022).
52. Tan, B. et al. Insight into anti-corrosion mechanism of tetrazole derivatives for X80 steel in 0.5 M H₂SO₄ medium: Combined experimental and theoretical researches. *J. Mol. Liq.* **321**, 114464 (2021).
53. Gao, L., Peng, S., Gong, Z. & Chen, J. A combination of experiment and theoretical methods to study the novel and low-cost corrosion inhibitor 1-hydroxy-7-azabenzotriazole for mild steel in 1 M sulfuric acid. *RSC Adv.* **8**, 38506–38516 (2018).
54. Liu, P. et al. Investigation of microstructure and corrosion behavior of weathering steel in aqueous solution containing different anions for simulating service environments. *Corros. Sci.* **170**, 108686 (2020).
55. Zhao, T., Liu, Z., Du, C., Sun, M. & Li, X. Effects of cathodic polarization on corrosion fatigue life of E690 steel in simulated seawater. *Int. J. Fatigue* **110**, 105–114 (2018).
56. Wu, W., Cheng, X., Zhao, J. & Li, X. Benefit of the corrosion product film formed on a new weathering steel containing 3% nickel under marine atmosphere in Maldives. *Corros. Sci.* **165**, 108416 (2020).
57. Freire, L., Carmezim, M. J., Ferreira, M. G. S. & Montemor, M. F. The electrochemical behaviour of stainless steel AISI 304 in alkaline solutions with different pH in the presence of chlorides. *Electrochim. Acta* **56**, 5280–5289 (2011).
58. Ma, H., Chen, L., Zhao, J., Huang, Y. & Li, X. Effect of prior austenite grain boundaries on corrosion fatigue behaviors of E690 high strength low alloy steel in simulated marine atmosphere. *Mater. Sci. Eng. A* **773**, 138884 (2020).
59. Dwivedi, D., Lepková, K. & Becker, T. Carbon steel corrosion: a review of key surface properties and characterization methods. *RSC Adv.* **7**, 4580–4610 (2017).
60. Rafiee, E., Farzam, M., Golzar, M. A. & Ashrafi, A. An investigation on dislocation density in cold-rolled copper using electrochemical impedance spectroscopy. *ISRN Corros.* **2013**, 921825 (2013).
61. Li, Z., Chen, J., Xue, W., Yin, C., Song, J. & Xiao, K. Role of segregation behavior of Cu and Sb in the region of inclusions on initial corrosion. *NPJ Mater. Degrad.* **7**, 29 (2023).
62. Ghahari, M. et al. Synchrotron X-ray radiography studies of pitting corrosion of stainless steel: Extraction of pit propagation parameters. *Corros. Sci.* **100**, 23–35 (2015).
63. Li, L., Li, X., Dong, C. & Huang, Y. Computational simulation of metastable pitting of stainless steel. *Electrochim. Acta* **54**, 6389–6395 (2009).
64. Ghahari, S. M. et al. In situ synchrotron X-ray micro-tomography study of pitting corrosion in stainless steel. *Corros. Sci.* **53**, 2684–2687 (2011).
65. Kong, D. et al. Surface monitoring for pitting evolution into uniform corrosion on Cu-Ni-Zn ternary alloy in alkaline chloride solution: ex-situ LCM and in-situ SECM. *Appl. Surf. Sci.* **440**, 245–257 (2018).
66. Tian, W., Li, S., Du, N., Chen, S. & Wu, Q. Effects of applied potential on stable pitting of 304 stainless steel. *Corros. Sci.* **93**, 242–255 (2015).
67. Wang, Y., Cheng, G., Wu, W., Qiao, Q., Li, Y. & Li, X. Effect of pH and chloride on the micro-mechanism of pitting corrosion for high strength pipeline steel in aerated NaCl solutions. *Appl. Surf. Sci.* **349**, 746–756 (2015).
68. Li, J. J. N. M. Diffusive origins. *Nat. Mater.* **14**, 656–657 (2015).
69. Yang, S. et al. Mechanism of the dual effect of Te addition on the localised corrosion resistance of 15–5PH stainless steel. *Corros. Sci.* **212**, 110970 (2023).
70. Bäbler, R. *Materials Handbook—A Concise Desktop Reference*. (2020).
71. Dong, C., Luo, H., Xiao, K., Ding, Y., Li, P. & Li, X. Electrochemical behavior of 304 Stainless steel in marine atmosphere and its simulated solution. *Anal. Lett.* **46**, 142–155 (2013).

ACKNOWLEDGEMENTS

The authors wish to acknowledge the National Nature Science Foundation of China [No. 52104319]; the National Science and Technology Resources Investigation Program of China (Grant No. 2019FY101400). The authors also want to thank Qinlin Li and Lianjun Hao in university of Science and Technology Beijing for their assistance in the measurements.

AUTHOR CONTRIBUTIONS

C. Liu, C. Li, and X. L. carried out the experiment. C. Liu and Z. C. wrote the manuscript with support from S.Y., Z. L. and X. C. Y. Z. provided graphing technique. All authors discussed the results.

COMPETING INTERESTS

The authors declare no competing interests.

ADDITIONAL INFORMATION

Correspondence and requests for materials should be addressed to Shufeng Yang.

Reprints and permission information is available at <http://www.nature.com/reprints>

Publisher's note Springer Nature remains neutral with regard to jurisdictional claims in published maps and institutional affiliations.



Open Access This article is licensed under a Creative Commons Attribution 4.0 International License, which permits use, sharing, adaptation, distribution and reproduction in any medium or format, as long as you give appropriate credit to the original author(s) and the source, provide a link to the Creative Commons license, and indicate if changes were made. The images or other third party material in this article are included in the article's Creative Commons license, unless indicated otherwise in a credit line to the material. If material is not included in the article's Creative Commons license and your intended use is not permitted by statutory regulation or exceeds the permitted use, you will need to obtain permission directly from the copyright holder. To view a copy of this license, visit <http://creativecommons.org/licenses/by/4.0/>.

© The Author(s) 2023